

Pyroelectrocatalytic CO₂ reduction for methanol driven by temperature-variation

Lingbo Xiao

Soochow University

Xiaoli Xu

Soochow University

Yanmin Jia (✉ jiayanmin@xupt.edu.cn)

Xi'an University of Posts and Telecommunications

Ge Hu

Soochow University

Jun Hu (✉ jhu@suda.edu.cn)

Soochow University <https://orcid.org/0000-0002-7575-2165>

Biao Yuan

ShanghaiTech University <https://orcid.org/0000-0001-9085-3928>

Yi Yu

ShanghaiTech University

Guifu Zou (✉ zouguifu@suda.edu.cn)

Soochow University

Article

Keywords: Pyroelectrocatalytic, CO₂ reduction, Temperature variation, Bismuth tungstate nanoplates

Posted Date: July 15th, 2020

DOI: <https://doi.org/10.21203/rs.3.rs-40906/v1>

License:   This work is licensed under a Creative Commons Attribution 4.0 International License.

[Read Full License](#)

Abstract

Taking the advantages of pyroelectric nanostructured materials, we use the temperature-variation, a ubiquitous phenomenon in our daily life, to reduce carbon dioxide (CO₂) for methanol through pyroelectrocatalytic process. Layered-perovskite bismuth tungstate nanoplates harvest heat energy from temperature-variation, driving pyroelectrocatalytic CO₂ reduction for methanol at temperatures between 15 °C and 70 °C. The methanol yield can be as high as 55.0 μmol·g⁻¹ after experiencing 20 cycles of temperature-variation. This efficient, cost-effective, and environmental-friendly pyroelectrocatalytic CO₂ reduction route provides a new thought towards utilizing natural diurnal temperature-variation for future methanol economy.

Introduction

For hundreds of years, fossil fuels have always been the main energy source for human activities and industrial manufacture. As the demand of the energy resource increases, the availability of fossil fuels and more release of carbon dioxide (CO₂) in atmosphere have raised serious concerns for the society. For instance, energy crisis, greenhouse effect, and ocean acidification are some of the major challenges faced by humankind¹⁻³. Converting CO₂ into hydrocarbon fuels is considered as one of the ideal solutions which can solve not only the environmental problems but also the high demand of energy consumption. Various methods have been explored to convert CO₂, such as photocatalytic reduction, electrocatalytic reduction, biological transformation, hydrogenation, and/or dry reforming⁴⁻⁷. Nevertheless, hydrogenation of CO₂ to form CH₃OH process requires high operating temperatures (200–250 °C) and high pressures (5–10 MPa), which limits the yield of methanol⁸. Photocatalytic reduction of CO₂ can be carried out in relatively mild temperature and pressure, but it always suffers insufficient light absorption and no response under dark condition⁹. Therefore, it is imperative to develop alternative, cost-effective, and environmentally friendly approach for CO₂ conversion.

Temperature variation is a recurrent phenomenon in our daily life¹⁰. The impact could be tremendous if we could harvest such abundant energy source during temperature variation. Such a motive is not unreasonable considering that pyroelectric materials can convert heat energy into electric energy via repeating cooling or heating process¹¹⁻¹³. Similar to the photocatalysis, pyroelectrocatalytic process can produce positive and negative charges by using pyroelectric materials as the active media during temperature variation. The energy generated through such a process has been applied to some catalytic process such as dye decomposition¹⁴⁻¹⁶ and water splitting^{17,18}. Theoretical calculation shows that a pyroelectric engine in an ideal condition can reach an energy conversion efficiency as high as 84-92%, which is much higher than the photovoltaic energy conversion efficiency typically in the range of 20%^{19,20}. Theoretically, Arvin Kakekhani *et al.* have approved the feasibility of pyroelectrocatalytic water splitting²¹. However, there is no report, based on our best knowledge, about collecting the energy using pyroelectric materials from temperature variation for CO₂ reduction.

The study of ferroelectrics' catalytic properties has been nearly seventy years. For example, the internal fields resulted from the polarization from the ferroelectrics can separate electrons and holes, thus enhance the catalytic efficiency¹⁷. Furthermore, ferroelectric polarization can affect molecular adsorption onto and desorption from the surface of the materials²¹. It is well known that all ferroelectric materials are pyroelectric materials. As the simplest member of bismuth layer-structured Aurivillius phase, bismuth tungstate (Bi_2WO_6) exhibits excellent ferroelectric and pyroelectric properties. Meanwhile, Bi_2WO_6 has some other interesting properties such as high ion conductivity, large spontaneous polarization ($P \cong 50 \mu\text{C}/\text{cm}^2$), high Curie temperature ($T_C = 950 \text{ }^\circ\text{C}$), and photocatalytic property^{22,23}. As Bi_2WO_6 is constructed by alternating $(\text{Bi}_2\text{O}_2)^{2+}$ and $(\text{WO}_4)^{2-}$ layers, such a layered structure enables high thermal and chemical stabilities²⁴. More importantly, the suitable energy band structure and surface properties of Bi_2WO_6 allow it for CO_2 reduction into renewable hydrocarbon fuel^{25,26}. In this work, we, for the first time in the community, report the use of pyroelectrocatalytic Bi_2WO_6 nanoplates to convert CO_2 into methanol by harvesting the energy from temperature variation below $100 \text{ }^\circ\text{C}$. The efficiency has reached as high as $55.0 \mu\text{mol}\cdot\text{g}^{-1}$ after experiencing 20 cycles between $15 \text{ }^\circ\text{C}$ and $70 \text{ }^\circ\text{C}$. Our experimental work provides a new route and key step to CO_2 reduction for methanol through a pyroelectrocatalytic process which can be carried out near room temperature.

Results And Discussion

Characterization of Bi_2WO_6 . Previous study shows that Bi_2WO_6 is ferroelectric with an orthorhombic structure, an intermediate phase with orthorhombic $B2cb$ structure above $670 \text{ }^\circ\text{C}$, and a monoclinic structure above $950 \text{ }^\circ\text{C}$ ²⁷. We synthesized Bi_2WO_6 nanoplates by a hydrothermal process (see the experimental details in the section of Materials and Methods). To confirm and identify the phase of the materials, X-ray diffraction (XRD) analysis was performed at room temperature. As shown in Fig. 1a, all the diffraction peaks can be assigned to Bi_2WO_6 according to the standard JCPDS card No. 79-2381 (space group: $Pca2_1$; point group: $mm2$; orthorhombic crystal system).

The morphology of as synthesized Bi_2WO_6 can be seen from the Fig. 1b, the Bi_2WO_6 shows nanoplate morphology with an average feature size of 250 nm. Fig. 1c presents the image of Bi_2WO_6 from transmission electron microscopy (TEM), where the nanoplate has the similar feature size as revealed by scanning electron microscope (SEM) shows in Fig. 1b. The high-resolution transmission electron microscopy (HRTEM) image of Bi_2WO_6 is shown in Fig. 1d. It clearly shows the single-crystalline nature of Bi_2WO_6 nanoplate with a lattice plane distances of 0.27nm, corresponding to the (002)/(200) plane, respectively. The aberration-corrected HAADF-STEM image of Bi_2WO_6 sample is presented in Fig. 1e. The light/dark gray contrast spots correspond to Bi ($Z = 83$, where Z is the atomic number) and W ($Z = 74$) atom columns, respectively. The inset image denotes the fast Fourier transformation (FFT) of the STEM image. The FFT image shows the zone axis of the STEM image is $[103]$, which is perpendicular to b direction. Therefore, the STEM image reflects the layered structure of Bi_2WO_6 , which is sandwiched by

alternating perovskite-like $(\text{WO}_4)^{2-}$ and fluorite-like $(\text{Bi}_2\text{O}_2)^{2+}$ blocks. A comparison between the STEM image and the structure model is schematically illustrated in Fig. 1f. The left picture in Fig. 1f is the magnified image of the area marked in red rectangle in Fig. 1e. The inset in Fig. 1e shows the simulated diffraction pattern in the [103] projection direction. Complete structure model is shown in the right side of Fig. 1f.

Bi_2WO_6 is paraelectric with a high-symmetry body-centered tetragonal structure (space group symmetry $I4/mmm$) at high temperature. When the temperature drops, symmetry of the crystal structure will be broken, the distortion of the symmetry tetragonal structure makes Bi_2WO_6 to generate ferroelectric properties. This mainly includes two aspects. Firstly, the ions displace along the [110] axis of the tetragonal structure. Secondly, the WO_6 octahedra rotate around the a and c axes²⁸. In order to characterize the ferroelectric properties of the as-synthesized Bi_2WO_6 nanoplates, Ferroelectric domains of Bi_2WO_6 nanoplates were observed using a piezoelectric force microscope (PFM) at a slow scanning frequency of 1 Hz with an area of $0.8 \times 0.8 \mu\text{m}^2$. The nanoplates morphology of Bi_2WO_6 shows in Fig. 2a is consistent with the result from TEM and SEM. Figs. 2b and 2c shows the vertical piezo-response amplitude and phase image, respectively. The distinct contrast in the images illustrates the different polarization in the Bi_2WO_6 nanoplates. Figs. 2d and 2e display the local piezoelectric hysteresis loops of the Bi_2WO_6 , including both “off” state (piezoelectric displacement contribution only) and “on” state (both the piezoelectric contribution and the displacement resulted from electrostatic interaction). The phase angles at “off” and “on” states change about 150° under 60 V DC bias field, confirming the occurrence of a local polarization switching under an electric field. The butterfly-shaped hysteresis loop further confirms the local ferro-/piezoelectric response of Bi_2WO_6 nanoplate.

It is noted that Bi_2WO_6 also shows pyroelectric properties, where imbalanced polarization charges can generate electric field when the material undergoes a temperature variation. The voltage produced by pyroelectric effect can be a driving force for electrochemical reaction. Fig. S1 shows the pyro-potential distribution across a Bi_2WO_6 nanoplate fitted by COMSOL finite element simulation, in which different colors represent different potentials. It can be seen potential difference occurs on the surfaces of the Bi_2WO_6 nanoplates. In general, ferroelectric materials have greater pyroelectric and piezoelectric coefficients than non-ferroelectrics²⁸. In order to confirm Bi_2WO_6 can generation pyroelectric charges through temperature variation, pyro-current response of Bi_2WO_6 nanoplates was measured. When the material is irradiated by the infrared light and accompanied with a rapid increase of temperature, the pyroelectric charges would be generated quickly due to the pyroelectric effect. The pyroelectric current can be expressed by the following Equation (1),

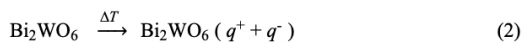
$$I_{\text{pyro}} = p \cdot A \cdot (dT/dt) \quad (1)$$

where A is the area of electrode, p is the pyroelectric coefficient, and dT/dt is the temperature change rate. Therefore, the pyroelectric current is proportional to dT/dt , and any change in temperature can generate

charges for pyroelectric materials. Fig. 2e shows the current dependent of the Bi_2WO_6 nanoplates on the infrared light signal. Fig. 2f shows the detailed response of the material to the light illumination. When the light is on, a sharp increase of current density is induced by the pyroelectric effect due to the rapid increase of temperature within Bi_2WO_6 nanoplates. The current density decays slowly due to the decrease of temperature, and maintains at a steady value under the equilibrium condition. A reversed current (negative current density shows in Fig. 2g) is generated due to the pyroelectric charges' re-distribution by instantaneous temperature decrease ($dT/dt < 0$) when the light is turned off. The output current returns to zero while there are no temperature change and light illumination. To confirm the temperature effect discussed above, we used xenon lamp (UV light), instead of the infrared light, to illuminate the sample. Under such circumstances, there was no pyro-current was generated (see Fig. S2).

Pyroelectrocatalytic activity of Bi_2WO_6 . To evaluate the pyroelectrocatalytic activity of Bi_2WO_6 , we use the temperature variation via the pyroelectric effect and apply such a method for CO_2 catalytic reduction activity. The methanol yield increases with the temperature-variation cycles as shown Fig. 3a. The total methanol yield reaches $20.5 \mu\text{mol}\cdot\text{g}^{-1}$ without adding any sacrificial agent after 20 temperature-variation cycles. The ^1H NMR in Fig. S3 also demonstrates that no other products can be detected in liquid phase. Meanwhile, the analyses of gaseous product in Fig. S4 show only a small amount of CH_4 and CO ($0.11 \mu\text{mol}\cdot\text{g}^{-1}$ and $0.20 \mu\text{mol}\cdot\text{g}^{-1}$, respectively), indicating high selectivity of Bi_2WO_6 pyroelectrocatalytic CO_2 reduction to CH_3OH . It has been similarly reported that the photocatalytic process can be reduced due to the recombination of electrons and holes. Such a process will significantly affect the catalytic efficiency^{29,30}. To reduce the occurrence of electrons recombination with holes, sacrificial agents are usually added to the reaction system. Fig. 3b shows that more methanol can be generated by using Na_2SO_3 as negative charge sacrificial agent. The methanol yield can be as high as $55.0 \mu\text{mol}\cdot\text{g}^{-1}$ after 20 temperature-variation cycles, which is 2.5 times more than that without Na_2SO_3 . It is also noted that the Bi_2WO_6 nanoplates maintain their crystal structure and morphology after pyro-catalytic reduction as confirmed by the XRD analysis and SEM characterization (see Fig. S5). For further proof that the CO_2 reduction comes from pyroelectrocatalysis, the result in Fig. S6a shows that no methanol or other products can be detected under temperature variation when experiments was performed without Bi_2WO_6 nanoplates. Furthermore, no methanol or other products can be detected in Fig. S6b when the test was run with the presence of Bi_2WO_6 nanoplates for 10 h at temperatures of 15°C , 45°C and 70°C , respectively. CO_2 is a linear molecule, which is one of the most thermodynamically stable carbon compounds, so it's hard to break the bonding of $\text{C}=\text{O}$ ^{8,31}.

To have a better understanding of the pyroelectric catalysis, O_2^- and $\cdot\text{OH}$ detection were performed. Pyroelectric charges can react with O_2 and OH^- in water to form superoxide anions (O_2^-) and hydroxyl radicals ($\cdot\text{OH}$). Such reactions can be expressed as the following equations,



Experimentally, the $\cdot\text{OH}$ can be detected by fluorescence spectrometry using terephthalic acid as a photoluminescent $\cdot\text{OH}$ trapping agent. The O_2^- can be detected by UV-vis spectrophotometer since O_2^- can react with nitro-blue tetrazolium (BNT) to produce diformazan and monoformazan. As shown in Fig. 3c, significant fluorescence emission at ~ 425 nm which is associated with 2-hydroxyterephthalic acid is observed upon the temperature-variation cycles. The gradual increase of luminescence intensity with temperature-variation cycles indicates the formation of hydroxyl radicals. Fig. 3d presents the absorption spectra of diformazan and monoformazan, which are produced by BNT reacted with O_2^- . The increase of peak absorption at ~ 630 nm and 720 nm with the temperature-variation cycles suggests the formation of superoxide anions³². The generation of both superoxide anions and hydroxyl radicals indicates the production of charges through pyroelectric catalytic reaction through temperature variation as illustrated by the reactions described by equations (2)-(4). Superoxide anions and hydroxyl radicals are considered to be the main active species in dye decomposition³³. Except for the pyroelectrocatalysis of CO_2 reduction, we further performed RhB pyroelectrocatalytic decomposition experiment to fully demonstrate the pyroelectrocatalytic activities. In fact, RhB pyroelectrocatalytic decomposition is a visual evidence to prove the redox ability of pyroelectric generated charges. Accordingly, Rhodamine B (RhB) solution (5 mg L^{-1}) is used to demonstrate the pyroelectrocatalytic dye decomposition of Bi_2WO_6 in Fig. S7a and S7b. In order to prove that methanol is the product of CO_2 reduction, we did the isotopic labeling experiment using $^{13}\text{CO}_2$ as feedstock. The ^1H NMR spectrum of the reaction solution (Fig. 3e) clearly shows the formation of methanol ($\delta=3.34$ ppm) when the unlabeled CO_2 is used as feedstock. While using $^{13}\text{CO}_2$ instead of CO_2 , the ^1H NMR spectrum of the reaction solution in Fig. 3f show doublet peaks between 3.7 and 3 ppm, which was attribute to the proton coupled to the ^{13}C of $^{13}\text{CH}_3\text{OH}$ ³⁴. The small peak of CH_3OH at 3.34 ppm possibly comes from the decomposed CO_2 of NaHCO_3 during the heating process, participating in CO_2 reduction³⁵. The results indicate that CO_2 is the carbon source for the pyroelectrocatalytic CO_2 reduction into CH_3OH .

Theoretical calculation of CO_2 reduction reaction path. To better understand the reaction mechanism for the CO_2 reduction, we carried out first-principles calculations with SIESTA package which is based on density functional theory (DFT)³⁶. The pseudopotentials were constructed by the Troullier-Martins scheme³⁷. The Ceperley-Alder exchange-correlation functional as parameterized by Perdew and Zunger was employed for the local density approximation (LDA)^{38,39}. In all calculations, the double- ζ plus polarization basis sets were chosen for all atoms. The atomic structures were fully relaxed using the conjugated gradient method until the Hellman-Feynman force on each atom is smaller than 0.02 eV/\AA . Since Bi_2WO_6 consists of alternative $(\text{WO}_4)^{2-}$ and $(\text{Bi}_2\text{O}_2)^{2+}$ layers as discussed above, a slab model is

constructed for the $\text{Bi}_2\text{WO}_6(001)$ surface. The top of the slab is terminated by the WO square network, and the bottom of the slab is saturated by H atoms, as shown in Fig. S8. It is known that oxygen vacancies commonly exist in oxide semiconductors⁴⁰. However, it is found that the formation energy of an oxygen vacancy in $\text{Bi}_2\text{WO}_6(001)$ is as large as 3.2 eV, which indicates that the density of oxygen vacancies in $\text{Bi}_2\text{WO}_6(001)$ is ignorable. To explore the possible process of the CO_2 reduction, it is necessary to figure out the ground-state adsorption configuration of the CO_2 molecule on $\text{Bi}_2\text{WO}_6(001)$. Fig. 4a shows five different adsorption configurations for CO_2 . The lowest adsorption energy is -3.6 eV, which implies that the CO_2 molecule is strongly bound to $\text{Bi}_2\text{WO}_6(001)$. In this case, the CO_2 molecule is bent with one C-W bond (2.00 Å) and two O-W bonds (2.09 and 2.26 Å) as shown in Fig. 4b (*step "0"*), which is different from previous report⁹. The C-O bond lengths are elongated by 0.1 Å, because of the interaction between CO_2 and $\text{Bi}_2\text{WO}_6(001)$. The CO_2 reduction starts when the hydrogen ions in the solvent interact with the CO_2 molecule. Note that DFT calculations, the hydrogen atom as proton (H^+) and electron (e^-) cannot be separated directly. To model the reaction between H and radical on $\text{Bi}_2\text{WO}_6(001)$, a H atom is placed beside a certain site of the radical and carried out DFT calculations to optimize the interaction between them. Electron charge transfer happens between the H atom and radical, usually from H to the radical so that the H atom finally becomes H^+ , according to the chemical bonding between H and the radical (e.g. CO_2 molecule in this work). In other words, charge separation can be reached after self-consistent-field iterations. In addition, the gas phase of H is assumed because the solvent does not involve in the reaction of the CO_2 reduction. The process of the CO_2 reduction is divided into a series of steps and the reaction energies are calculated step by step. All possible structural configurations along with addition of one H ion are considered for each step simulation. For instance, from step "0" to step "1", the H ion may bind to the CO_2 molecule through C or O atom, or to the $\text{Bi}_2\text{WO}_6(001)$ surface through W or O atoms, which results in different products. To determine the most possible reaction, the reaction energy of each product is estimated as: $\Delta E = E(n) - E(n - 1) - \mu_{\text{H}}$, where $E(n)$ is the total energy of a certain product at the n th step and μ_{H} is the chemical potential of H. After optimizing all structural configurations, we pick up the case with the lowest reaction energy at each step and plotted the optimized structural configuration in Fig. 4b. Obviously, the structural configurations in Fig. 4b are the most possible products for each step. The reaction energy of the most possible product at each step is plotted in Fig. 4c. Here, the first three H ions at the first three steps prefer to bind to the C atom, and these reactions are exothermic due to the large negative reaction energies as seen in Fig. 4c. As a consequence, one C-O bond is broken and a CH_3O^* radical and a separate O ion are produced at *step "3"*. Then the subsequent H ions will be attracted by the separated O ion until a H_2O molecule forms (*step "5"*). However, the H_2O molecule is not released from $\text{Bi}_2\text{WO}_6(001)$, because it requires a large activation energy of about 1.7 eV. Finally, a methanol (CH_3OH) molecule is produced after one more H ion attaches to the CH_3O^* radical (*step "6"*). As shown in Fig. 4c, the first four reaction steps are exothermic while the last three are endothermic. In particular, an activation energy of 1.6 eV (equal to the reaction energy) is needed for the CH_3OH molecule to be detached from the $\text{Bi}_2\text{WO}_6(001)$ surface, i.e. from *step "6"* to *step "7"*. Note that CH_3OH may also be produced at *steps "4"* and *"5"* (short dashed lines in Fig. 4c), but the

corresponding activation energies are respectively 1.77 and 1.87 eV, even larger than that for *step* "7". Therefore, the possibility to produce CH₃OH at *steps* "4" and "5" is very small, because the major reactions at the first two steps are exothermic. Nevertheless, the overall process of the CO₂ reduction is still exothermic as shown in Fig. 4c, that is, the activation energies in the last three reaction steps can be compensated by the energy released in the first four steps. Hence the CO₂ reduction lasts spontaneously in principle. Nevertheless, given the energy loss in a solvent environment, energy supply is still needed but the energy demanding is not much. This is the reason that the temperature is not high in our experiments. It is worth pointing out that, when the CH₃OH molecule is detached from the Bi₂WO₆ (001) surface, the zero-point energy and enthalpy contribute to the free energy significantly⁴¹. Therefore, the reaction energies are also estimated through the free energies for CH₃OH production indicated by the red lines in Fig. 4c. Interestingly, the activation energy of *step* "7" decreases to 0.95 eV, which implies that the reaction may happen at relatively high temperature, as found in our experiments.

On the basis of above analysis, a mechanism of pyroelectrocatalytic CO₂ reduction induced by pyroelectric Bi₂WO₆ nanoplates is proposed in Fig. 5. When the catalyst temperature remains in a stable value, the internal spontaneous polarization balances with the external bound charges (Fig. 5a). It has been reported that the polarization density relies on the temperature of the pyroelectrocatalyst⁴². That is to say, the increase of temperature would lower the polarity of the pyroelectrocatalyst, so that the balance is broken and the free charges are generated. The free negative charges react with adsorbed CO₂ to form methanol and the free positive charges would be captured by Na₂SO₃ to form Na₂SO₄ (Fig. 5b). As a result, a new balance is established between polarization and bonding charges (Fig. 5c). On the other hand, the decrease of temperature caused the increase of spontaneous polarization, and the equilibrium will be broken again, thus leading to opposite charges transfer and new CO₂ reduction process (Fig. 5d). The next balance is established to return the original state between polarization and bonding charges, so temperature variation will continuously produce the pyroelectrocatalytic behavior of CO₂ conversion into methanol.

In summary, a new approach for efficient CO₂ reduction is introduced by pyroelectrocatalytic Bi₂WO₆ nanoplates during temperature variation. Experimental result shows that the yield of methanol generation from CO₂ can be as high as 55.0 μmol·g⁻¹ after 20 cycles of temperature variation. This efficient and environment friendly process based on the pyroelectric nanomaterial Bi₂WO₆ provides great potential for CO₂ reduction in utilizing environmental heat energy near room-temperature.

Materials And Methods

Materials. All used chemicals are analytic grade reagents without further purification. Bismuth nitrate (Bi(NO₃)₃·5H₂O, AR), sodium tungstate (Na₂WO₄·2H₂O, AR) and sodium bicarbonate (NaHCO₃, AR), dimethyl sulfoxide (DMSO, AR) were acquired from Sinopharm Chemical Reagent Co., Ltd. Sodium sulfite (Na₂SO₃, AR) was purchased from Shanghai Macklin Biochemical Co., Ltd. Carbon dioxide (CO₂,

$\geq 99.995\%$) was purchased from Soochow Jinhong Co., Ltd. Deuterium oxide (D_2O , $\geq 99.9\%$) was purchased from Qingdao Asfirst Science and trade Co., Ltd. $^{13}CO_2$ was bought from Soochow changyou gas Co., Ltd with purity of 99.9%. Deionized water was employed throughout the whole experiments.

Preparation of Bi_2WO_6 nanoplates. Bi_2WO_6 nanoplates were synthesized through hydrothermal process. In a typical process, 485 mg of $Bi(NO_3)_3 \cdot 5H_2O$ (1 mmol) and 165 mg of $Na_2WO_4 \cdot 2H_2O$ (0.5 mmol) were added into the mixed solution. White precipitate appeared immediately in the solution. After being washed for several times, the collected precipitate was added into a 50 mL Teflon-lined autoclave and filled with deionized water up to 80% of the total volume. Then the autoclave was sealed into a stainless steel tank and kept at 433 K for 20 h. After reactions, the white as-prepared sample was centrifugated with a speed of 6000 rpm and washed three times with deionized water. Finally, the collected products were dried in vacuum at 333 K for 12 h for further use.

Characterization. The crystal structure was test by an X-ray diffractometer (Philips PW3040/60, the Netherlands) with monochromatic Cu $K\alpha$ radiation ($\lambda=1.5406 \text{ \AA}$, $2\theta=20^\circ-80^\circ$). The morphologies of the Bi_2WO_6 sample was characterized by a transmission electron microscope (TEM, Hitachi H-7650, Japan) and a field emission transmission electron microscopy (FETEM, Scios, USA) with an accelerated voltage of 200 kV. The high resolution transmission electron microscopy (HRTEM) image was acquired through a field emission transmission electron microscopy (FEI Tecnai G2 F20 S-TWIN, USA) with the accelerated voltage of 200 kV. Aberration-corrected high-angle annular dark field scanning transmission electron microscopy (HAADF-STEM) image was obtained on a 300kV aberration-corrected JEM-ARM300F. The piezoelectric property of the Bi_2WO_6 sample was characterized with piezoresponse force microscopy (PFM, MFP-3D, USA). Photoluminescence (PL) measurements were carried out with a Horiba spectrofluorometer (Fluoromax-4, France) in air. Pyro-current response was measured on a CHI 660E electrochemical workstation using a three-electrode cell. The UV-visible absorption spectra are recorded on a UV2501PC (Shimadzu, Japan).

Pyro-catalytic CO_2 reduction activity test. In the pyroelectrocatalytic CO_2 conversion process, Bi_2WO_6 powder (40 mg) was suspended in 5 mL 0.2 M $NaHCO_3$ solution in a 35 mL borosilicate tube with the addition of 0.3 M Na_2SO_3 as a sacrificial donor. High purity CO_2 gas was bubbled into the borosilicate tube for 10 min. Then the tube was immediately sealed with a rubber stopper. Then the tube was immediately sealed with a rubber stopper. The sample was suspended in the solution under stirring, being applied alternating temperature between 15 °C and 70 °C in water bath. The entire catalytic process is performed in dark. The detailed temperature profile can be found from Fig. S9. To detect the formation of methanol, 1 mL solution was fetched out and analyzed by using a gas chromatograph (Persee G5) equipped with a KB-5 column connected to a flame ionization detector. For the nuclear magnetic resonance (NMR) test, 800 μ L reaction solution, 100 μ L D_2O and 10 μ L DMSO (0.1% vol aqueous solution) were taken into nuclear magnetic tubes, and detected with an NMR spectrometer with superconducting magnet (AVANCE NEO 400MHz, Switzerland).

Declarations

Acknowledgements

We gratefully acknowledge the support from the National Natural Science Foundation of China (21971172, 21671141, 11574223), the Natural Science Foundation of Jiangsu Province (BK20150303), the Priority Academic Program Development (PAPD) of Jiangsu Higher Education Institutions for Optical Engineering, the Center for High-resolution Electron Microscopy (ChEM) at ShanghaiTech University, and Jiangsu Collaborative Innovation Center of Photovoltaic Science and Engineering.

Author contributions:

G. Z. and Y. J. conceived the project and idea. L. X. and X. X. carried out the experiment and process data. G. H. and J. H. perform the theoretical calculations. Y. Y. and B. Y. carried out the STEM. All authors participated in the formulation of the paper.

Competing interests: The authors declare no competing interests.

References

1. Wei, J. et al. Directly converting CO₂ into a gasoline fuel. *Nat. Commun.* **8**, 15174 (2017).
2. Zhang, L., Zhao, Z. J. & Gong, J. Nanostructured materials for heterogeneous electrocatalytic CO₂ reduction and their related reaction mechanisms. *Angew. Chem. Int. Ed. Engl.* **56**, 11326-11353 (2017).
3. Rodriguez, J. A. et al. Hydrogenation of CO₂ to methanol: Importance of metal-oxide and metal-carbide interfaces in the activation of CO₂. *ACS Catal.* **5**, 6696-6706 (2015).
4. Bard, A. J. & Fox, M. A. Artificial photosynthesis-solar splitting of water to hydrogen and oxygen. *Acc. Chem. Res.* **28**, 141-145 (1995).
5. Bai, S. et al. Highly active and selective hydrogenation of CO₂ to ethanol by ordered Pd-Cu nanoparticles. *J. Am. Chem. Soc.* **139**, 6827-6830 (2017).
6. Lin, S. et al. Covalent organic frameworks comprising cobalt porphyrins for catalytic CO₂ reduction in water. *Science* **349**, 1208-1213 (2015).
7. Wu, J. et al. Efficient visible-light-driven CO₂ reduction mediated by defect-engineered BiOBr atomic layers. *Angew. Chem. Int. Ed. Engl.* **57**, 8719-8723 (2018).
8. Du, X. L., Jiang, Z., Su, D. S. & Wang, J. Q. Research Progress on the Indirect Hydrogenation of Carbon Dioxide to Methanol. *ChemSusChem* **9**, 322-332 (2016).
9. Tu, W., Zhou, Y. & Zou, Z. Photocatalytic conversion of CO₂ into renewable hydrocarbon fuels: state-of-the-art accomplishment, challenges, and prospects. *Adv. Mater.* **26**, 4607-4626 (2014).
10. Lang, S. B. & Muensit, S. Review of some lesser-known applications of piezoelectric and pyroelectric polymers. *Appl. Phys. A* **85**, 125-134 (2006).

11. Pandya, S. et al. Pyroelectric energy conversion with large energy and power density in relaxor ferroelectric thin films. *Nat. Mater.* **17**, 432-438 (2018).
12. Pandya, S. et al. New approach to waste-heat energy harvesting: pyroelectric energy conversion. *NPG Asia Mater.* **11** (2019).
13. Wang, Q. et al. Hexagonal boron nitride nanosheets doped pyroelectric ceramic composite for high-performance thermal energy harvesting. *Nano Energy* **60**, 144-152 (2019).
14. Xu, X. et al. Strong pyro-electro-chemical coupling of Ba_{0.7}Sr_{0.3}TiO₃@Ag pyroelectric nanoparticles for room-temperature pyrocatalysis. *Nano Energy* **50**, 581-588 (2018).
15. Wu, J. et al. Strong pyro-catalysis of pyroelectric BiFeO₃ nanoparticles under a room-temperature cold-hot alternation. *Nanoscale* **8**, 7343-7350 (2016).
16. Qian, W. et al. Thermo-electrochemical coupling for room temperature thermocatalysis in pyroelectric ZnO nanorods. *Electrochem. Commun.* **81**, 124-127 (2017).
17. Xu, X. et al. Pyro-catalytic hydrogen evolution by Ba_{0.7}Sr_{0.3}TiO₃ nanoparticles: harvesting cold-hot alternation energy near room-temperature. *Energy Environ. Sci.* **11**, 2198-2207 (2018).
18. You, H. et al. Room-temperature pyro-catalytic hydrogen generation of 2D few-layer black phosphorene under cold-hot alternation. *Nat. Commun.* **9**, 2889 (2018).
19. Sebald, G., Pruvost, S. & Guyomar, D. Energy harvesting based on Ericsson pyroelectric cycles in a relaxor ferroelectric ceramic. *Smart Mater. Struct.* **17**, 015012 (2008).
20. Olsen, R. B. & Evans, D. Pyroelectric energy-conversion-hysteresis loss and temperature sensitivity of a ferroelectric material. *J. Appl. Phys.* **54**, 5941-5944 (1983).
21. Kakekhani, A. & Ismail-Beigi, S. Ferroelectric oxide surface chemistry: water splitting *via* pyroelectricity. *J. Mater. Chem. A* **4**, 5235-5246 (2016).
22. Djani, H., Bousquet, E., Kellou, A. & Ghosez, P. First-principles study of the ferroelectric Aurivillius phase Bi₂WO₆. *Phys. Rev. B* **86** (2012).
23. Djani, H., Hermet, P. & Ghosez, P. First-principles characterization of the *P2₁ab* ferroelectric phase of Aurivillius Bi₂WO₆. *J. Phys. Chem. C* **118**, 13514-13524 (2014).
24. Liang, L. et al. Single unit cell bismuth tungstate layers realizing robust solar CO₂ reduction to methanol. *Angew. Chem. Int. Ed. Engl.* **54**, 13971-13974 (2015).
25. Zhou, Y. et al. High-yield synthesis of ultrathin and uniform Bi₂WO₆ square nanoplates benefitting from photocatalytic reduction of CO₂ into renewable hydrocarbon fuel under visible light. *ACS Appl. Mater. Interfaces* **3**, 3594-3601 (2011).
26. Cheng, H. et al. An anion exchange approach to Bi₂WO₆ hollow microspheres with efficient visible light photocatalytic reduction of CO₂ to methanol. *Chem. Commun.* **48**, 9729-9731 (2012).
27. McDowell, N. A., Knight, K. S. & Lightfoot, P. Unusual high-temperature structural behaviour in ferroelectric Bi₂WO₆. *Chem. Eur. J.* **12**, 1493-1499 (2006).

28. Machado, R., Stachiotti, M. G., Migoni, R. L. & Tera, A. H. First-principles determination of ferroelectric instabilities in Aurivillius compounds. *Phys. Rev. B* **70** (2004).
29. Wang, R., Ni, S., Liu, G. & Xu, X. Hollow CaTiO₃ cubes modified by La/Cr co-doping for efficient photocatalytic hydrogen production. *Appl. Catal. B-Environ.* **225**, 139-147 (2018).
30. Xu, G. et al. Integrating the g-C₃N₄ nanosheet with B-H bonding decorated metal-organic framework for CO₂ activation and photoreduction. *ACS Nano* **12**, 5333-5340 (2018).
31. Yang, R., Yu, X., Zhang, Y., Li, W. & Tsubaki, N. A new method of low-temperature methanol synthesis on Cu/ZnO/Al₂O₃ catalysts from CO/CO₂/H₂. *Fuel* **87**, 443-450 (2008).
32. Liu, R.-h., Fu, S.-y., Zhan, H.-y. & Lucia, L. A. General Spectroscopic Protocol to Obtain the Concentration of the Superoxide Anion Radical. *Ind. Eng. Chem. Res.* **48**, 9331–9334 (2009).
33. Akram, N. et al. Synergistic Catalysis of Co(OH)₂/CuO for the Degradation of Organic Pollutant Under Visible Light Irradiation. *Sci Rep* **10**, 1939 (2020).
34. Sekizawa, K., Maeda, K., Domen, K., Koike, K. & Ishitani, O. Artificial Z-scheme constructed with a supramolecular metal complex and semiconductor for the photocatalytic reduction of CO₂. *J. Am. Chem. Soc.* **135**, 4596-4599 (2013).
35. Zhang, S., Kang, P. & Meyer, T. J. Nanostructured tin catalysts for selective electrochemical reduction of carbon dioxide to formate. *J. Am. Chem. Soc.* **136**, 1734-1737 (2014).
36. SanchezPortal, D., Ordejon, P., Artacho, E. & Soler, J. M. Density-functional method for very large systems with LCAO basis sets. *Int. J. Quantum Chem.* **65**, 453-461 (1997).
37. Troullier, N. & Martins, J. L. Efficient pseudopotentials for plane-wave calculations. *Phys. Rev. B* **43**, 1993-2006 (1991).
38. Ceperley, D. M. & Alder, B. J. Ground state of the electron gas by a stochastic method. *Phys. Rev. Lett.* **45**, 566-569 (1980).
39. Perdew, J. P. & Zunger, A. Self-interaction correction to density-functional approximations for many-electron systems. *Phys. Rev. B* **23**, 5048-5079 (1981).
40. Hu, J. & Pan, B. C. The optical and vibrational properties of dominant defects in undoped ZnO: A first-principles study. *J. Appl. Phys.* **105**, 083710 (2009).
41. Peterson, A. A., Abild-Pedersen, F., Studt, F., Rossmeisl, J. & Norskov, J. K. How copper catalyzes the electroreduction of carbon dioxide into hydrocarbon fuels. *Energy Environ. Sci.* **3**, 1311-1315 (2010).
42. Zhang, Y. et al. Thermal Energy Harvesting Using Pyroelectric-Electrochemical Coupling in Ferroelectric Materials. *Joule* **4**, 301-309 (2020).

Figures

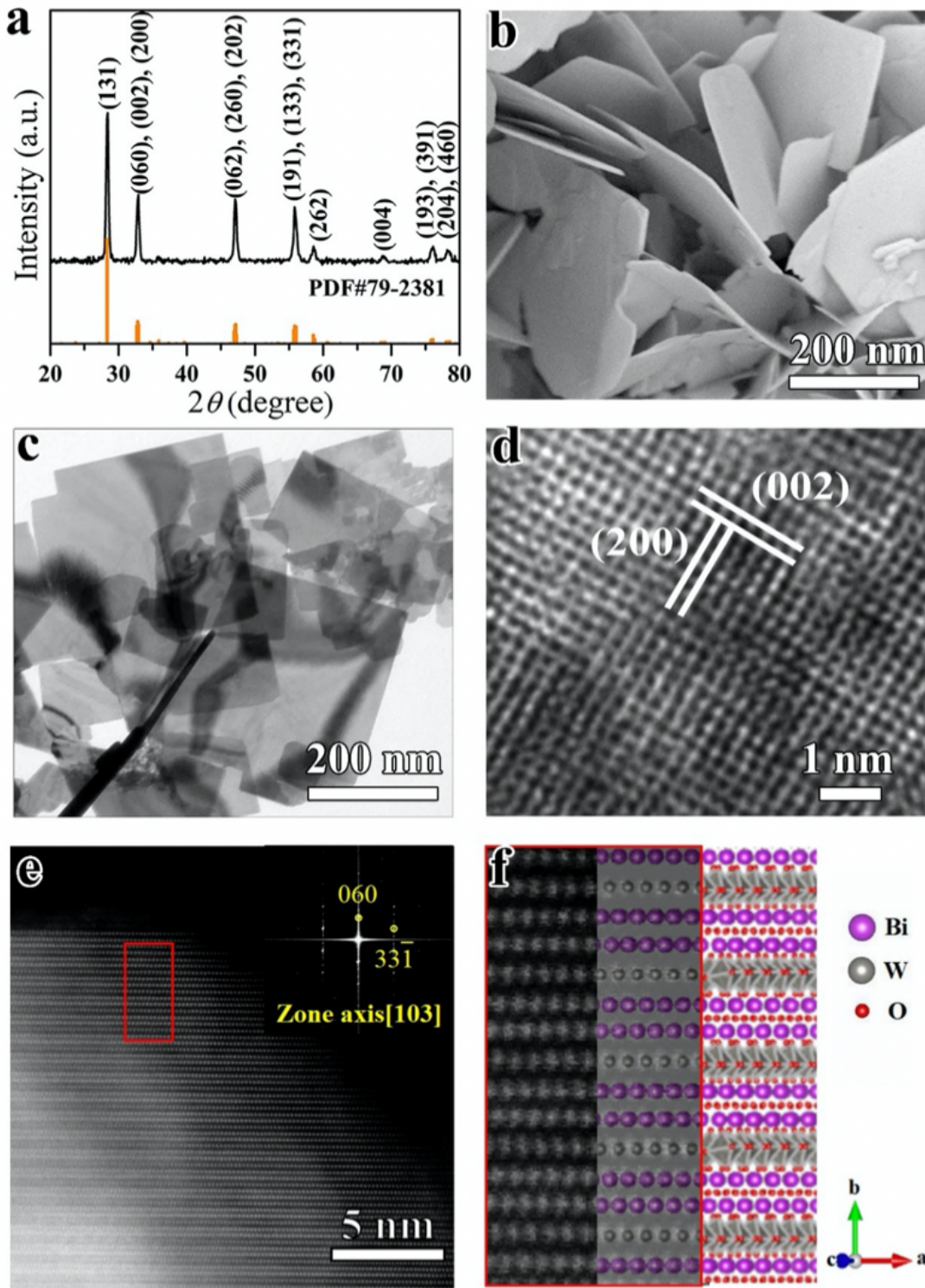


Figure 1

Structures of Bi_2WO_6 sample. (a) XRD pattern, (b) SEM photograph, (c) TEM photograph, (d) HRTEM image, and (e) Aberration-Corrected HAADF-STEM image. The inset image in (e) denotes the FFT of STEM. (f) Comparison between the STEM image and the structure model of the layered-structure of Bi_2WO_6 .

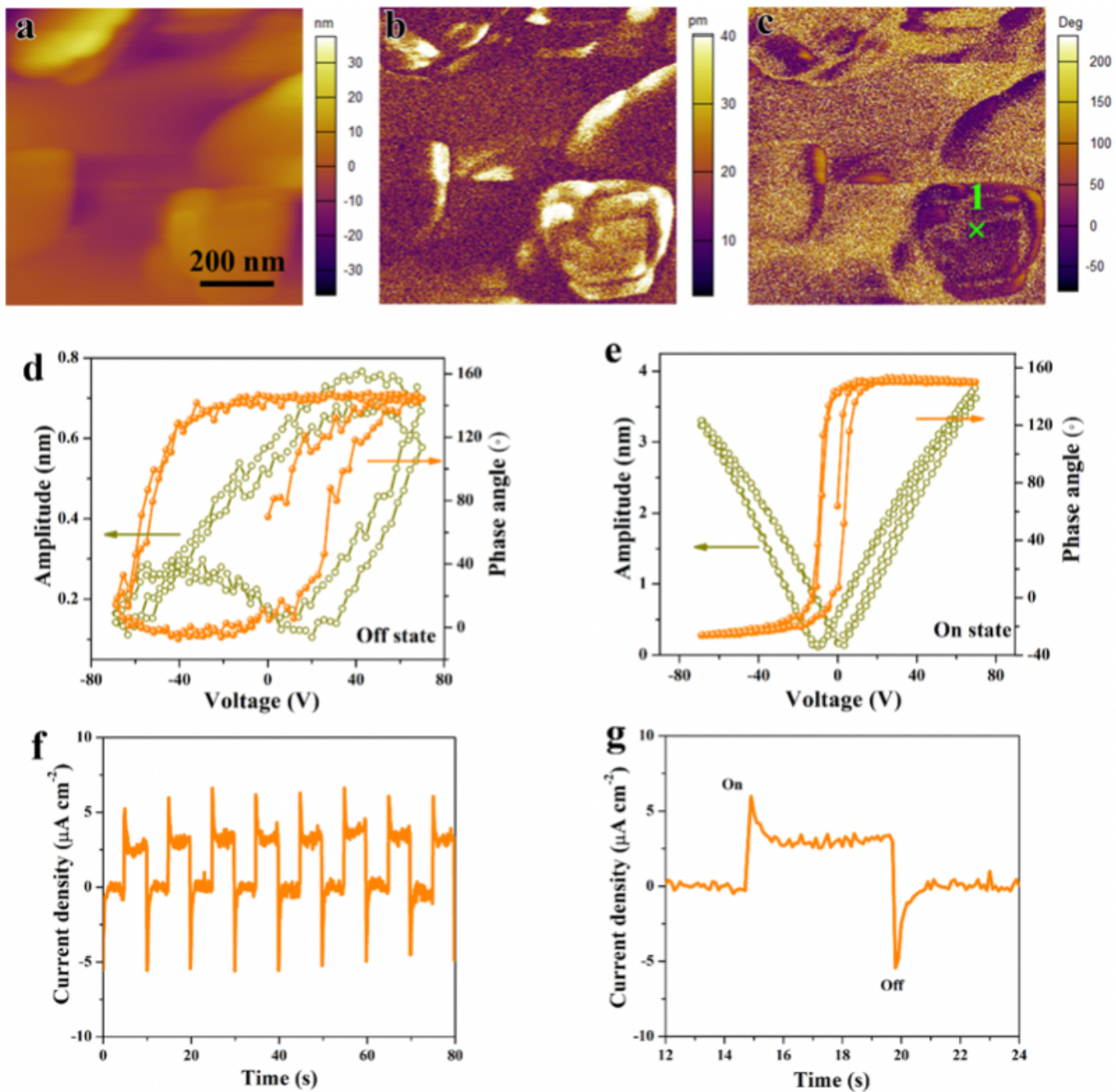


Figure 2

Ferro-/Pyro-electric properties of Bi₂WO₆. (a) topology, (b) vertical amplitude, and (c) phase images of Bi₂WO₆ nanoplate. The local hysteresis loops of Bi₂WO₆ nanoplate for point 1 marked in (c): (d) “off” state, and (e) “on” state. (f) The Pyro-current response of Bi₂WO₆, (g) enlarged view of one full light on/off cycle is shown in Fig. f.

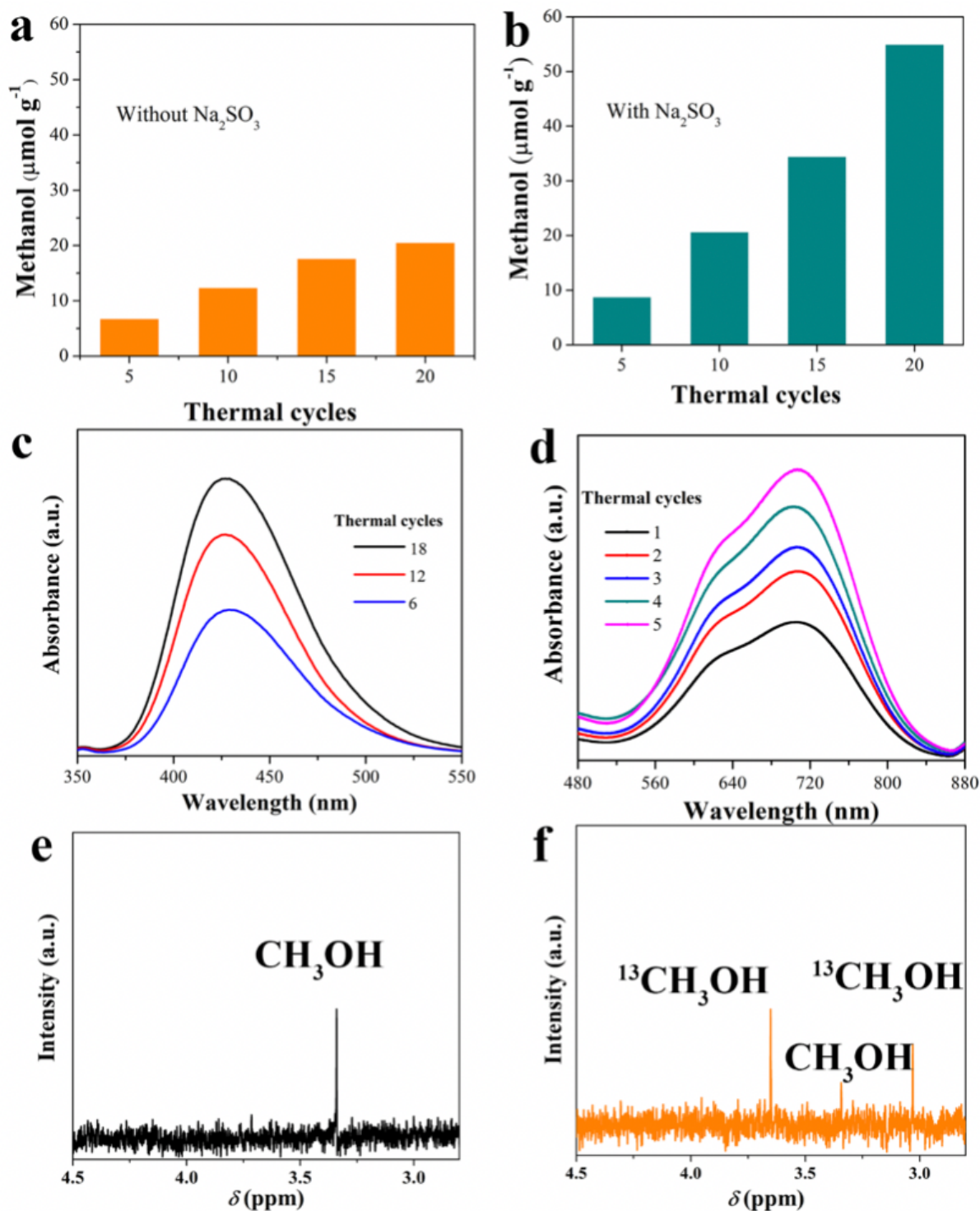


Figure 3

Catalytic activities of Bi_2WO_6 . (a) methanol yield through pyroelectrocatalytic CO_2 conversion without Na_2SO_3 , and (b) with Na_2SO_3 as sacrificial agent. (c) The fluorescence spectra of 2-hydroxyterephthalic acid, (d) The absorption spectra of diformazan and monoformazan. (e) ^1H NMR spectra of the pyroelectrocatalytic reaction solution with unlabeled CO_2 and (f) ^1H NMR spectra of the pyroelectrocatalytic reaction solution with labeled $^{13}\text{CO}_2$.

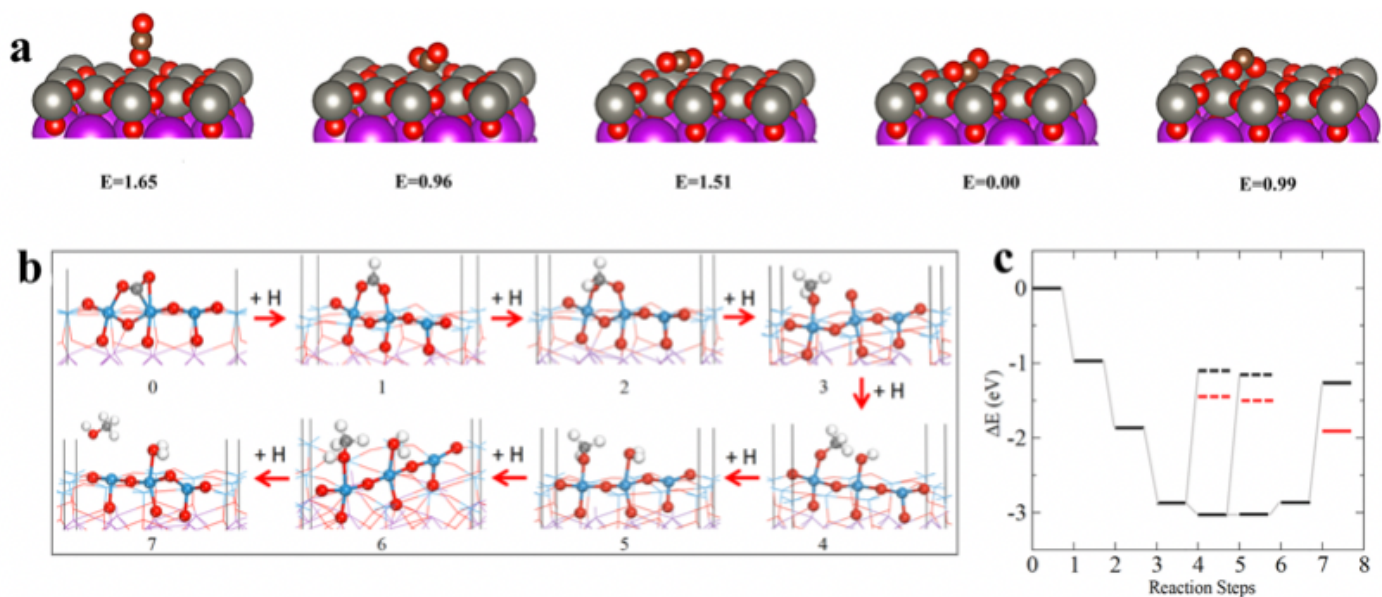


Figure 4

Adsorption configurations and reaction path of CO₂ into CH₃OH on Bi₂WO₆. (a) Five different adsorption configurations for CO₂ on Bi₂WO₆. (b) Structures and (c) reaction energies for the CO₂ reduction. Eight reaction steps are considered. The red, cyan, light grey and dark grey spheres stand for O, W, Bi, H and C atoms. Only the atoms around CO₂ are highlighted. The reaction energies for the side product (methanol) at steps “4” and “5” are indicated by short dashed lines. The short red (dashed) lines are estimated from the free energies.

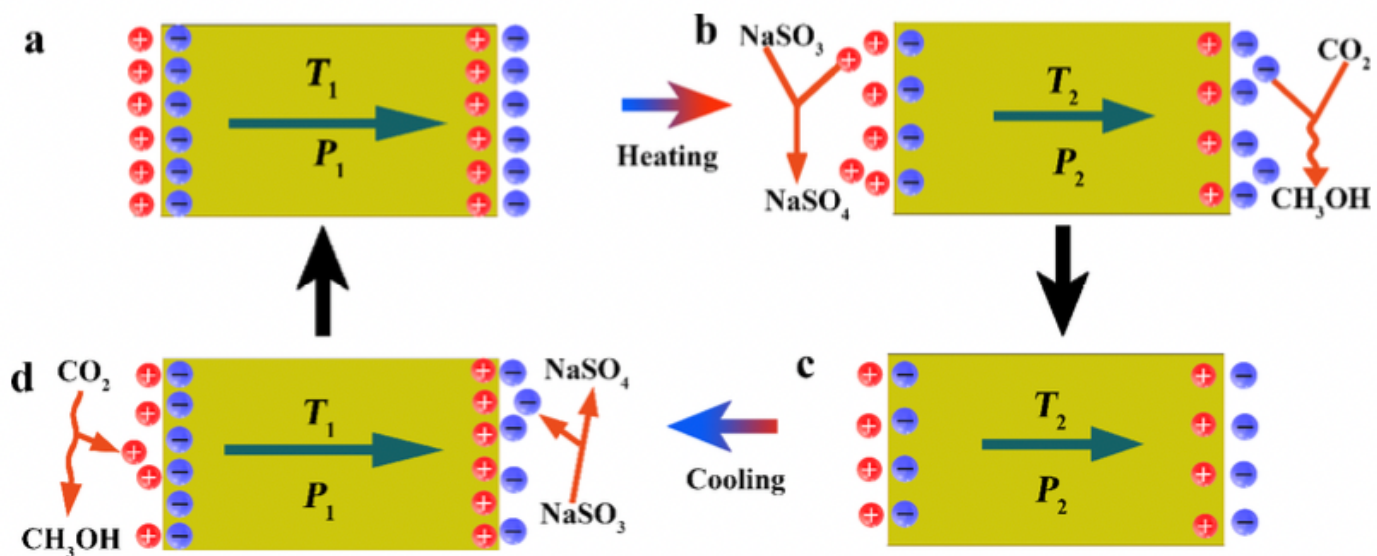


Figure 5

The mechanism of pyro-catalytic CO₂ reduction induced by pyroelectric Bi₂WO₆ nanoplate. (a) The catalyst temperature remains in a stable value, spontaneous polarization is in equilibrium with the bound charges. (b) The rapid rise in temperature broke the balance, and thus induce CO₂ reduction reaction. (c) A new balance is established after the CO₂ reduction reaction. (d) When the temperature drops, the opposite charges transfer leading to a new CO₂ reduction process.

Supplementary Files

This is a list of supplementary files associated with this preprint. Click to download.

- [SupplementaryInformation.docx](#)
- [GraphicalAbstract.png](#)